coatings

MDPI

Article

Co-O-Al Interfacial Bonding in Sol–Gel-Derived Co_3O_4-Coated Ceramic Membranes: Correlative FIB-HRTEM and First-Principles Analysis

Jia Xu [1], Wei Qiu [1,*] and Jingjing Yao [2]

[1] State Key Laboratory of Urban-Rural Water Resources and Environment, Harbin Institute of Technology, Harbin 150090, China; 22b929027@stu.hit.edu.cn
[2] Center for Environment and Water Resources, College of Chemistry and Chemical Engineering, Central South University, Changsha 410083, China; yaojj0412@163.com
* Correspondence: qiuwei@hit.edu.cn

Abstract

Co-based oxides are commonly introduced into porous ceramic membranes to add catalytic activity, but their attachment at the atomic scale remains unclear. We examined a buried Co_3O_4/Al_2O_3 interface formed by sol–gel deposition and thermal conversion. Site-specific focused-ion-beam (FIB) lift-out, scanning transmission electron microscopy with energy-dispersive X-ray spectroscopy (STEM-EDS), and high-resolution transmission electron microscopy (HRTEM) were used to access and characterize the interface. A Co-rich spinel-type domain with a (111) lattice spacing was observed next to Al_2O_3(012). The observations guided density functional theory (DFT) initial models. After structural relaxation, substrate-O-mediated Co-O contacts emerged from both starting geometries: the O-bridged-start model exhibited eight contacts across four Co sites, whereas the non-bridged-start model developed three contacts around one Co site. Around the Co-O-Al linkages, there is a clear manifertation of the interface polarization and charge redistribution, indicated by charge-density-difference and Bader analyses. In both models, projected density of states (PDOS) showed coupling between Co 3d and O 2p states, while integrated crystal orbital Hamilton population (ICOHP) analysis further indicated that O atoms retained Al-O bonds while forming occupied-state Co-O bonds. These results support a representative, laterally distributed Co-O-Al motif as an atomic-scale pathway for chemically attaching the functional oxide to porous alumina.

Keywords: catalytic ceramic membranes; sol–gel coating; water treatment; cobalt oxide; alumina; buried interface; focused-ion-beam; density functional theory; interfacial chemical bonding

Check for updates

Academic Editor: Michal Krbat'a

Received: 10 August 2026
Revised: 29 August 2026
Accepted: 1 September 2026
Published: 3 September 2026

Copyright: © 2026 by the authors. Licensee MDPI, Basel, Switzerland. This article is an open access article distributed under the terms and conditions of the Creative Commons Attribution (CC BY) license.

1. Introduction

Porous ceramic membranes are increasingly being developed as catalytic media rather than purely as separation media [1–3]. When the active phase is immobilized on the outer surface or pore wall, the same porous matrix can combine physical separation and chemical conversion [4,5]. Recent tests have demonstrated that the catalytic phase can be applied to the ceramic membrane platform at the pilot scale [6]. From a coating perspective, successful functionalization requires not only the preservation of catalytic activity but also the durable adhesion of the active phase to the porous substrate.

Transition-metal oxides are among the most widely used active phases in catalytic ceramic membranes [7]. Their multivalent metal centers and lattice oxygen can activate oxidants and sustain redox cycles [8–10]. Oxide catalysts have been loaded onto porous ceramic membranes by solution impregnation, filtration-assisted loading, and hydrothermal synthesis [11,12]. Sol–gel processing provides another route, offering a advantage by controlling the precursors, reducing the reliance on the particle-size restriction and pressurized growth conditions [13–15]. In these methods, the functional phase may be retained by pore confinement, van der Waals attraction, direct interfacial chemical bonding, or a combination of these mechanisms [16–20]. Compared with interfaces stabilized by van der Waals interactions, the formation of interfacial chemical bonds generally results in stronger local binding [21]. While the catalytic performance of functionalized ceramic membranes has been extensively studied, a fundamental understanding of interfacial chemical bonds between oxides and ceramic remain less explored. To examine this interfacial bonding issue, the Co_3O_4/Al_2O_3 system was selected as a representative platform. Co_3O_4 is a typical catalyst for persulfate activation, whereas porous Al_2O_3 is a well-established ceramic membrane substrate [22,23].

Previous studies have inferred Co-O-Al connectivity from X-ray Photoelectron Spectroscopy (XPS), Raman spectroscopy, X-ray Diffraction (XRD), Co K-edge extended X-ray absorption fine structure (EXAFS) analyses, and suppressed cobalt leaching [19,22,24,25]. Nevertheless, these ensemble-averaging techniques fail to uniquely resolve the atomic-scale topology of specific shared-oxygen bridges at the buried interface. XPS analyses are inherently constrained by fitting models and charging effects, while Co 2p spectra suffer from multiplet splitting and shake-up satellites [26,27]. Moreover, bulk-sensitive methods cannot ascertain whether a substrate oxygen retains an Al-O bond while simultaneously forming a Co-O bond.

In this study, we investigated how the oxide catalytic layer adhered to the porous Al_2O_3 ceramic membrane. With the help of site-specific FIB lift-out, we isolated a buried Co_3O_4/Al_2O_3 junction from the functionalized membrane and examined it using STEM-EDS and HRTEM. Guided by the microscopy observations, we constructed two CoO_x/Al_2O_3 interface models with identical compositions. One model was initialized with substrate oxygen bridging the interface, and the other without predefined bridges. After structural relaxation, we determined whether the surface oxygen of Al_2O_3 could serve as a shared ligand connecting the cobalt oxide functional phase and the membrane substrate by combining charge density redistribution, PDOS analysis, and ICOHP analysis. Together, the results support a Co-O-Al motif based on shared oxygen. This work offers an atomic-scale insight for the interface of sol–gel-derived catalytic membranes, providing potential assistance for the rational design of functional catalytic membranes.

2. Materials and Methods

2.1. Preparation of the Functionalized Porous Ceramic Membrane

A porous Al_2O_3 ceramic membrane (47 mm in diameter, with an average pore size of about 1 μm) served as the substrate. Before coating, the membrane was washed with Milli-Q water(Milli-Q IQ 7005, Sigma-Aldrich, Wuxi, China) and ethanol. To prepare the cobalt-containing precursor, 29.10 g of cobalt nitrate, 9.61 g of citric acid, and 6.43 g of ethylene glycol were dissolved in 200 mL of Milli-Q water. The mixture was heated at 90 °C for 5 h. The resulting gel was coated onto the membrane at 500 rpm using a spin coater (Spin Master51, Chemat Advanced Ceramics Technology Co., Ltd., Shanghai, China). The modified membrane was dried at 90 °C for 12 h in an oven. The dried membrane was then calcined in a muffle furnace at 700 °C for 4 h. After cooling, the membrane was rinsed and soaked in Milli-Q water.

2.2. FIB Lift-Out of the Buried Interface and Subsequent Transmission Electron Microscopy (TEM) Characterization

Site-specific FIB-SEM lift-out was used to extract a lamella containing the buried Co_3O_4 interface using a Helios 5 UX FIB-SEM (Helios 5 UX DualBeam, Thermo Fisher Scientific, Waltham, MA, USA) equipped with a Ga^+ ion source, as shown in Figure 1. A target region containing the Co_3O_4/Al_2O_3 interface was identified manually in the SEM image. To prevent damage to the surface during ion milling, a Pt protective cap was deposited through the gas-injection system (GIS). Trenches were milled at 30 kV and 20 nA, followed by rough cutting at 30 kV and 10 nA and U-shaped cutting at 30 kV and 2.5 nA to isolate the interface-containing section. Then, the interface sheet was welded to the nanomanipulator using Pt and gently lifted and attached to a Cu TEM grid post. The lamella was thinned at 30 kV using successively lower beam currents of 250, 150, and 100 pA. Finally, low-energy cleaning was performed at 5 kV and 20 pA to reduce surface damage. The resulting lamella had an estimated thickness of about 70–80 nm and was subsequently used for TEM observation.

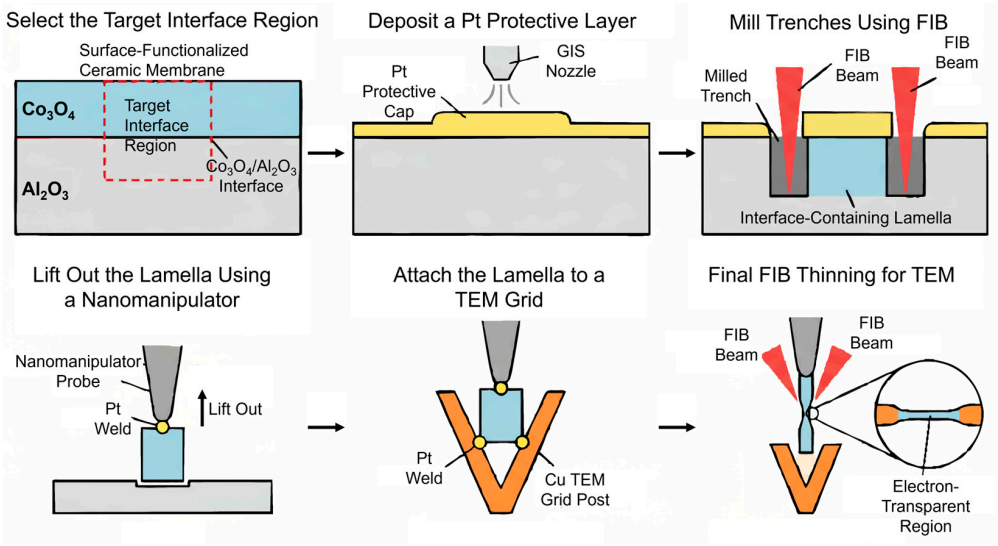


Figure 1. Site-specific FIB lift-out workflow used to isolate a buried Co_3O_4/Al_2O_3 junction from the functionalized porous ceramic membrane for further analyses.

The FIB-prepared lamella was characterized using a Talos F200X transmission electron microscope (Thermo Fisher Scientific, MA, USA) operated at an accelerating voltage of 200 kV. STEM imaging was performed using a high-angle annular dark-field (HAADF) detector. STEM-EDS elemental mapping was employed to examine the spatial distributions of Co, Al, and O across the interface. HRTEM was further employed to resolve the crystallographic relationship between the Co-rich region and the A_2O_3 substrate. The bulk phase of the coating layer was characterized by X-ray diffraction (XRD; X'Pert PRO, PANalytical, Almelo, The Netherlands).

2.3. First-Principles Calculations and Bonding-Structure Analyses

The parent crystal structures of spinel Co_3O_4 and Al_2O_3 were obtained from the Materials Project database using mp-18748 and mp-1143. The Co-containing component was generated by geometrically extracting a finite local Co-O fragment. Using a lateral extent of about 3.8 Å and a vertical extent of about 5.5 Å around the selected local Co-centered region resulted in a fragment containing 11 Co and 18 O atoms. On the substrate side, the $Al_{44}O_{72}$ component was obtained by removing four Al atoms from a $2 \times 2 \times 1$ real-space supercell [28]. The resulting $Al_{44}O_{90}Co_{11}$ composition contained 145 atoms. The

periodic DFT supercell was electronically neutral, with no electrons added to or removed from the system. Subsequent DFT calculations were performed using VASP [29,30]. The interface-facing part of the Al_2O_3 is O-terminated, whereas the opposite vacuum-facing side of the slab is Al-terminated [31,32]. During geometry optimization, 50 atoms were fixed, and 95 atoms were allowed to relax. On the Al_2O_3 side, the bottom 40 substrate atoms (16 Al and 24 O), corresponding to the lowest six atomic planes, were fixed to retain the underlying substrate framework. On the Co-containing side, 10 atoms in the upper part of the finite fragment (4 Co and 6 O) were fixed to preserve the bulk-derived framework at the finite-fragment boundary, whereas the Co and O atoms close to the interface were allowed to relax. The relaxation cell was a = b = 9.62 Å and c = 33.22 Å. The free space above the Co-containing fragment was about 11 Å. A dipole correction along the surface-normal direction was applied. The interactions between the ionic cores and valence electrons were described using the projector-augmented-wave method, and the exchange–correlation functional was treated within the Perdew–Burke–Ernzerhof generalized-gradient approximation [33–35]. Localized Co 3d correlations were treated using the Dudarev DFT + U formulation [36]. The Coulomb and exchange parameters enter through the effective interaction (U_{eff} = U−J). An effective Hubbard parameter of U_{eff} = 3.3 eV (U = 3.3 eV and J = 0 eV) was applied to the Co 3d states, consistent with previous studies of cobalt oxides and Co_3O_4 [37–39]. No Hubbard correction was applied to the Al or O states. The plane-wave cutoff energy was set to 520 eV. Geometry optimizations were carried out using Γ-point sampling. The electronic self-consistent iterations were converged to 1×10^{-5} eV, and structural relaxation was continued until the residual forces on the relaxed atoms were below 0.03 eV/Å. For the subsequent PDOS calculation, a denser Γ-centered ($2 \times 2 \times 1$) k-point mesh and a tighter electronic convergence criterion of 1×10^{-6} eV were employed.

The interaction energy was calculated as

$$E = E_{CoO_x - Al_2O_3} - E_{CoO_x} - E_{Al_2O_3} \quad (1)$$

where $E_{CoO_x - Al_2O_3}$ represents the total energy of the optimized models. E_{CoO_x} and $E_{Al_2O_3}$ are the energies of the CoO_x fragment and Al_2O_3 slab. For each relaxed interface model, the charge-density difference was evaluated as

$$\Delta\rho(r) = \rho_{interface}(r) - \rho_{Co_{11}O_{18}}(r) - \rho_{Al_{44}O_{72}}(r). \quad (2)$$

For each relaxed interface structure, the $Co_{11}O_{18}$ and $Al_{44}O_{72}$ reference fragments were generated directly from the corresponding relaxed interface by removing the complementary atoms while retaining the same supercell and the atomic coordinates. No additional structural relaxation was performed for either reference fragment. The interface and fragment charge densities were evaluated on the same $144 \times 144 \times 588$ fine FFT grid.

Bader charge analysis was additionally performed to provide an atom-resolved descriptor. The net Bader charge was defined as

$$q_{Bader} = Z_{val} - N_{Bader}, \quad (3)$$

where N_{Bader} is the number of electrons assigned to the Bader basin and Z_{val} is the PAW valence-electron count.

The overall magnitude of electron redistribution at the interface was calculated as

$$Q_{abs} = \int \left| \Delta\rho(r) \right| dr. \quad (4)$$

Plane averaging over the interfacial area A gave the charge-density-difference profile along the interface normal:

$$\Delta\bar{\rho}(z) = (1/A)\int_A \Delta\rho(x, y, z)dxdy. \quad (5)$$

The cumulative charge displacement was further defined as

$$Q(z) = A\int_{z_0}^{z} \Delta\rho(z')dz'. \quad (6)$$

PDOS calculations used the atom- and orbital-projection functions implemented in VASP, with LORBIT = 11 and NEDOS = 3000. For each model, the energy scale was referenced to its own Fermi level as the zero point:

$$E - E_F = 0. \quad (7)$$

In the PDOS plots, positive and negative values denote the spin-up and spin-down channels, respectively.

ICOHP and COHP analyses of the O-bridged-start model were performed using LOBSTER 4.1.0 to quantify the occupied-state bonding contributions [40,41]. The local basis used the pbeVaspFit2015 set and included Al 3s and 3p, O 2s and 2p, and Co 3d, 4s, and 4p orbitals. The interaction-distance ranges were set to 1.55–2.45 Å for Co-O pairs and 1.55–2.15 Å for Al-O pairs. The energy range used for the COHP analysis was −10 to 5 eV. The absolute charge-spilling values were 0.79% and 0.95% for the two channels, respectively, indicating a low loss of occupied-state density during projection onto the local basis. For the spin-polarized calculation, the reported -ICOHP value for each atomic pair was obtained by summing the contributions from the two spin channels.

3. Results

3.1. Element Distribution at the Co/Al Interface

After the cross-sectional lamella was extracted by FIB lift-out, EDS mappings were performed, as shown in Figure 2. In Figure 2a, at low magnification, the continuous distribution of the Al signal in the cross section is assigned to the Al_2O_3 membrane substrate. The O signal is detected throughout the target region. By contrast, Co is concentrated in discrete zones, owing to infiltration of the Co-containing precursor into the pores and cracks during the membrane preparation. The high-magnification mappings (Figure 2b) demonstrate a Co-rich band in direct contact with the Al_2O_3 substrate. The O signal remains detectable across both the Co- and Al-containing regions, and no obvious oxygen-free gap or non-oxide isolation layer is observed. Because both Co_3O_4 and Al_2O_3 are oxides, the continuously distributed oxygen element across this region does not by itself establish a specific Co-O-Al bridge.

3.2. Buried Interface and Local Crystallographic Relationship

TEM was conducted to examine the Co-rich region and the adjacent Al_2O_3 substrate in greater detail (Figure 3). Figure 3a contains obvious crystallization regions (B1 and B2) and a local interface (C) at the junction. To examine the local crystallographic relationship on either side of the junction, lattice-fringe measurements were performed in Figure 3b. In region B1, the measured spacing is approximately 3.469 Å, close to the d-spacing of α-Al_2O_3(012) in JCPDS No. 04-007-9625. Region B2 exhibits a spacing of approximately 4.697 Å, which is compatible with the (111) reflection of a Co-rich cubic spinel phase. As Co_3O_4 and Co-Al spinels possess very similar lattice parameters, it is necessary to take

into account the synthesis and compositional context. The deposited gel contained a Co precursor but no Al precursor, whereas Al was supplied only by the pre-existing Al_2O_3 ceramic substrate. Previous comparative studies have shown that transition-metal alumunate formation is substantially less facile on α-Al_2O_3 than on γ-Al_2O_3, for which cation penetration can occur at considerably lower temperatures [42]. More directly, some other studies suggest no detectable $Co_{3-x}Al_xO_4$ formation was observed for Co_3O_4 supported on the α-Al_2O_3 carrier under experimental conditions [43]. In addition, HRTEM shows two crystalline domains meeting directly at the buried junction, without a resolvable third crystalline interlayer. Considering the bulk phase is Co_3O_4, the single-phase observed by HRTEM is more likely to be Co_3O_4 (JCPDS No. 04-007-8056; Figure A1). Taken together, these observations favor Co_3O_4 as the principal cobalt-rich spinel phase under the present preparation conditions.

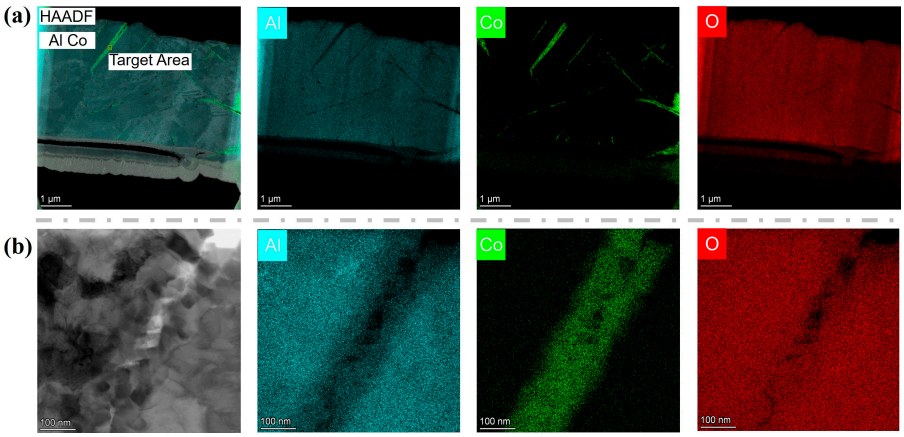


Figure 2. STEM-EDS maps of the extracted functionalized-membrane cross-section at (**a**) low and (**b**) high magnification.

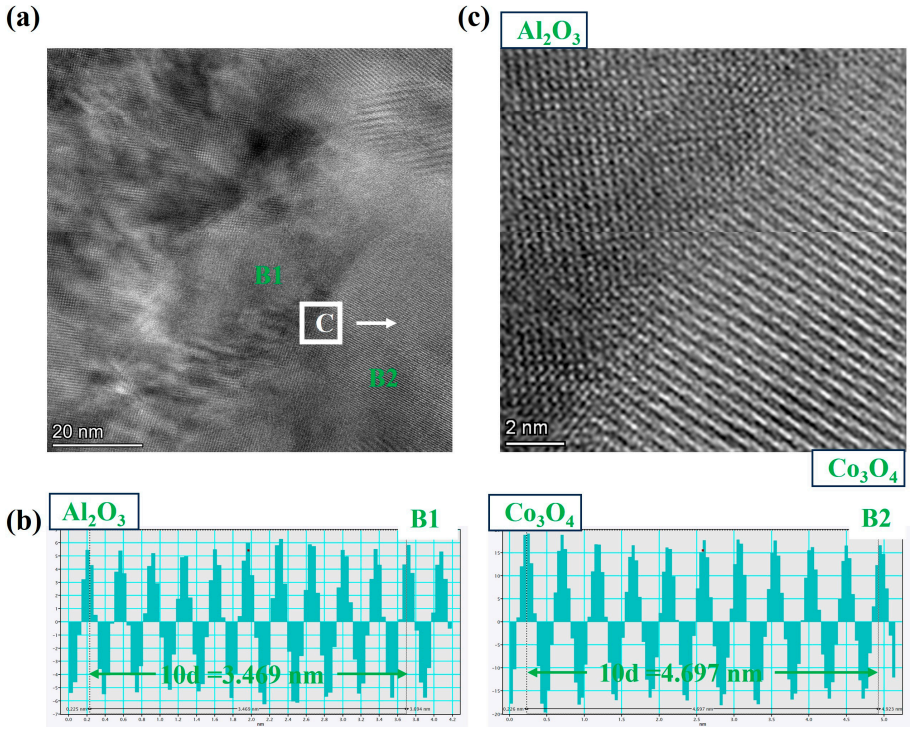


Figure 3. (**a**) HRTEM image, (**b**) interplanar spacings, and (**c**) local contact between the Co-rich spinel-type and Al_2O_3.

3.3. CoO_x/Al_2O_3 Interface Models

STEM-EDS and HRTEM mainly reflect the elemental distribution and lattice structure of the Co_3O_4/Al_2O_3 junction, but they do not by themselves identify the specific bonding mode. In the preparation process, a Co-containing gel was deposited directly on the Al_2O_3 substrate and then decomposed and crystallized, rather than mechanically attaching pre-formed Co_3O_4 grains. Previous studies have demonstrated surface-dependent interactions and grafting behavior of Co species on the Al_2O_3 surface, while epitaxial Co_3O_4 growth on Al_2O_3 has been related to the structural compatibility of their oxygen sublattices [44,45]. These observations support the chemical plausibility of substrate-O-mediated interfacial coordination. The surface O atoms on Al_2O_3 may act as coordination sites for Co species and form Co-O-Al bridges rather than direct Co-Al bonds. We therefore used DFT calculations to test this hypothesis through structural relaxation, charge redistribution, and bonding analyses using two distinct initial interface geometries. As illustrated in Figure 4, two local CoO_x/Al_2O_3 atomistic models were constructed to test whether substrate oxygen could act as a shared ligand between the Co-containing phase and the alumina framework. In the O-bridged-start model, an interfacial Co atom at the bottom of the CoO_x fragment was positioned near a surface O atom of Al_2O_3 to represent a substrate-O-mediated contact. The non-bridged-start model served as a control with no Co-O-Al bridge initially. It was obtained by translating the CoO_x fragment from the O-bridged-start position and lifting 0.80 Å along the interface normal, thereby removing the initial O-bridge contact. The two models contain the same number and types of atoms. The non-bridged-start model was not constrained to remain noninteracting, and relaxation was allowed to determine whether local Co-O-Al contacts formed from a geometry without a preset bridge.

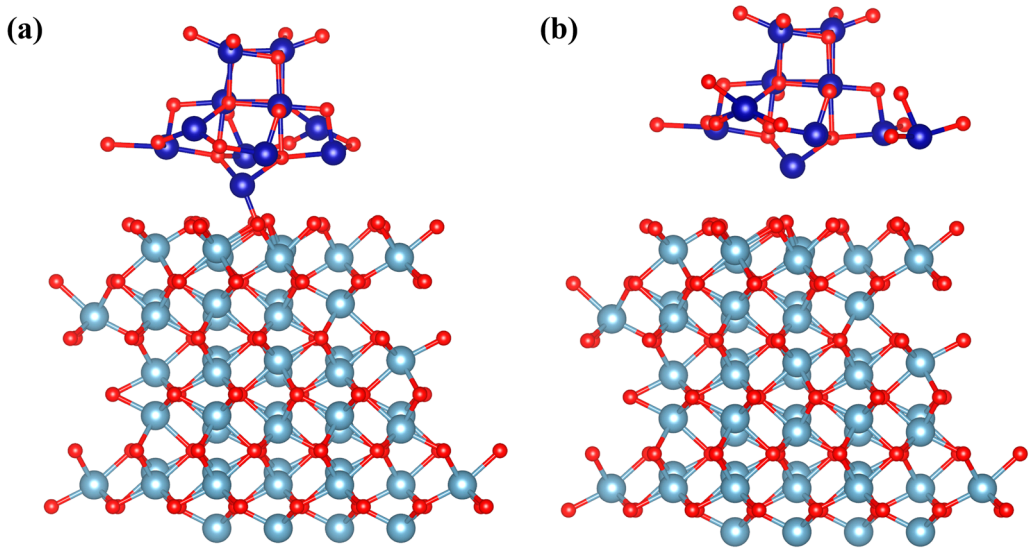


Figure 4. Initial (**a**) O-bridged-start and (**b**) non-bridged-start CoO_x/Al_2O_3 interface models derived from the local crystallographic relationship observed by HRTEM. Red, purple, and gray spheres denote O, Co, and Al, respectively.

3.4. Substrate-O-Mediated Contact Formation After Structural Relaxation

Both starting models were relaxed, and in each structure, the interfacial Co atoms moved into contacts with the surface O atoms of Al_2O_3 (Figure 5). The number of Co-O contacts increased from an initial value of 1 to 8 in the O-bridged-start model and from 0 to 3 in the non-bridged-start model. This indicates that there is an inherent tendency for interfacial Co atoms to form short-range coordination with the surface oxygen on the substrate. The initial O-mediated bridges can expand this coordination from a small number of local contacts (non-bridged-start model) to multiple interfacial sites (O-bridged-start

model). In the O-bridged-start model, Co136, Co139, Co142, and Co145 all approached the Al_2O_3 surface and established connections with one or more surface oxygen atoms. Co136 contacted O71, O78, and O83, Co145 contacted O69, O77, and O81, and Co139 and Co142 contacted O78 and O84, respectively. By comparison, only Co136 moved toward the substrate and coordinated with O71, O78, and O81, while the other interfacial Co atoms remained far from the substrate. Clearly, the O-bridged-start model developed a laterally distributed, multipoint Co-O contact network, whereas the non-bridged-start model retained a more localized contact. Furthermore, we calculated the interaction energies of both models. The reference energy is −958.21 eV, and the interaction energies are −980.181 eV for the O-bridged-start model and −976.057 eV for the non-bridged-start model. The lower interaction energies in both configurations indicate that the formation of Co-O-Al linkages from either start is spontaneous.

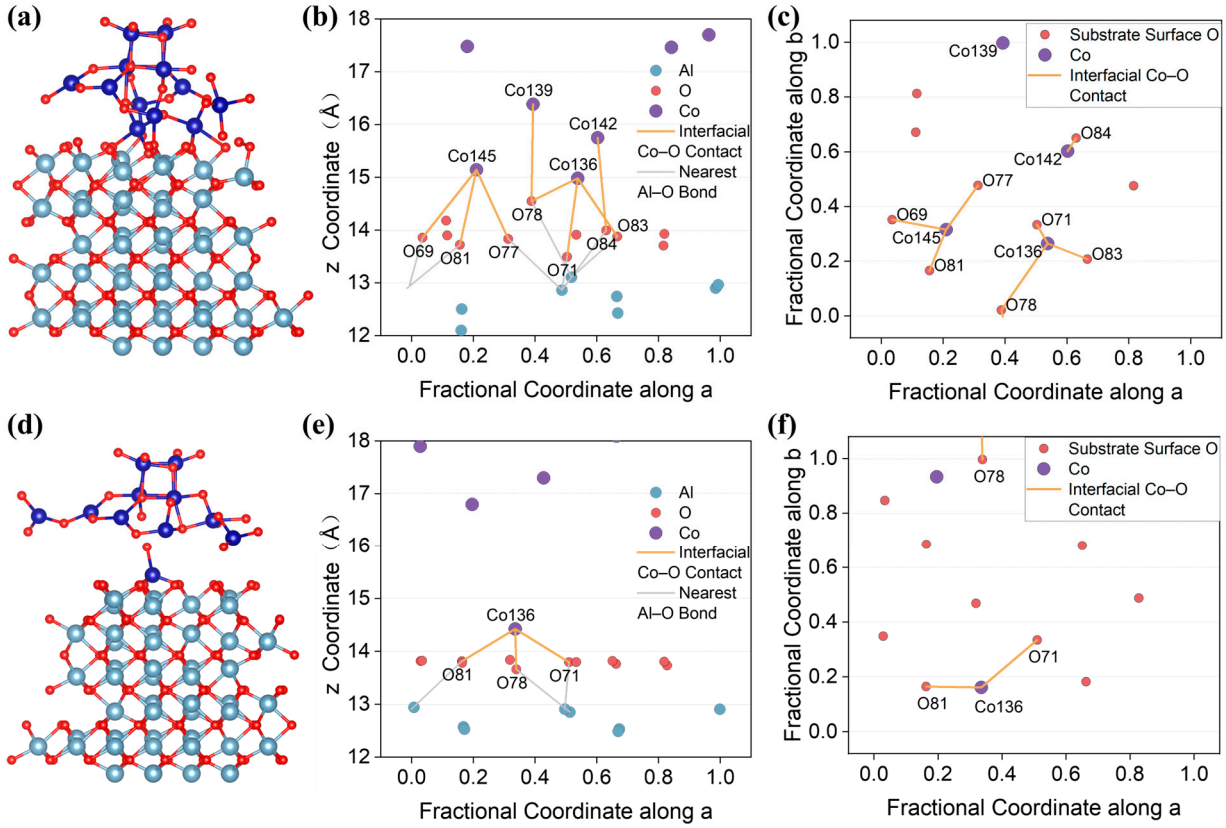


Figure 5. The optimized structures of the O-bridged-start and non-bridged-start models (**a**,**d**), together with the corresponding side views (**b**,**e**) and top views (**c**,**f**).

3.5. Interfacial Charge Rearrangement and Polarization

The charge-density-difference maps reveal that electronic redistribution is concentrated primarily around the interfacial Co-O contact regions (Figure 6). In the O-bridged-start model (Figure 6a), electron accumulation and depletion extend across several interfacial Co atoms and surface O atoms, producing a continuous polarization pattern along the junction. In the non-bridged-start model (Figure 6b), the redistribution is concentrated around the local coordination site. Bader analysis provides additional information on this redistribution (Table 1). In the O-bridged-start model, the four interfacial Co sites exhibit net Bader charges of +1.44 e, +1.15 e, +1.20 e, and +1.37 e. The substrate O atoms involved in the interfacial linkages exhibit values ranging from −0.85 e to −1.17 e. In the non-bridged-start model, Co 136 has a Bader charge of +1.34 e, while O71, O78, and O81 have values of −0.99 e, −1.02 e, and −0.94 e.

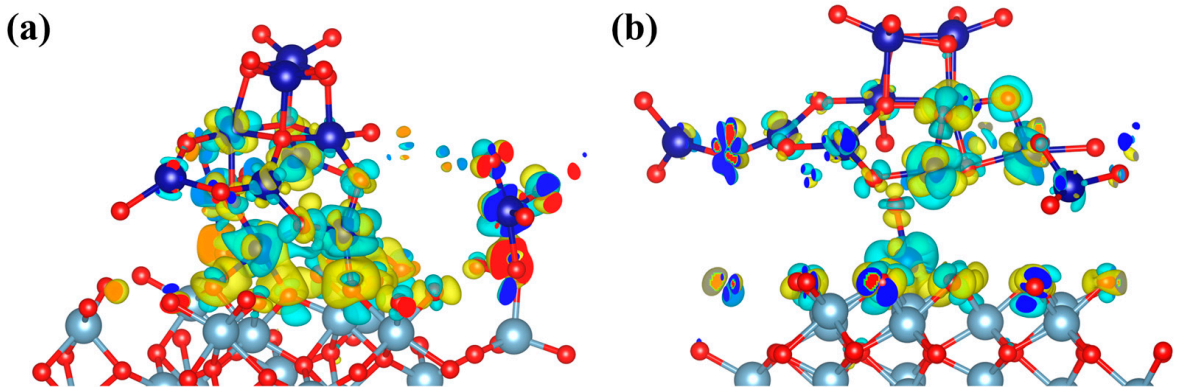


Figure 6. Three-dimensional charge-density-difference distributions for the relaxed (**a**) O-bridged-start and (**b**) non-bridged-start models. Yellow and cyan isosurfaces denote electron accumulation and depletion, respectively.

Table 1. Bader charges for the two relaxed interface models.

Model	Atom	q_{Bader} (e)
O-bridged-start	Co 136	+1.44
	Co 139	+1.15
	Co 142	+1.20
	Co 145	+1.37
	O 69	−0.95
	O 71	−1.03
	O 77	−1.05
	O 78	−0.85
	O 81	−1.17
	O 83	−0.98
	O 84	−0.99
non-bridged-model	Co 136	+1.34
	O 71	−0.99
	O 78	−1.02
	O 81	−0.94

3.6. Substrate O 2p-Mediated Orbital Coupling Across the Interface

To analyze the interaction at the orbital level, we calculated the PDOS for the relaxed structures (Figure 7). Figure 7a presents the spin-resolved PDOS of interfacial Co 3d, bridging substrate O 2p, and surface Al s/p states in the O-bridged-start model. It is clear that the occupied O 2p and Co 3d features overlap over a broad energy range, consistent with Co-O orbital coupling across the interface. A similar overlap appears in the relaxed non-bridged-start model (Figure 7b), where a local substrate-O-mediated contact also forms. In both models, no direct Co-Al hybridization is evident in the plotted PDOS, and the orbital coupling between the Al_2O_3 and interfacial Co is mainly established through the substrate O 2p states. Figure 7c,d compare representative O and Co sites with their reference states. Coordination changes the PDOS lines of both the bridging O atom and its neighboring Co atom across the occupied-energy range, consistent with changes in their local electronic environments.

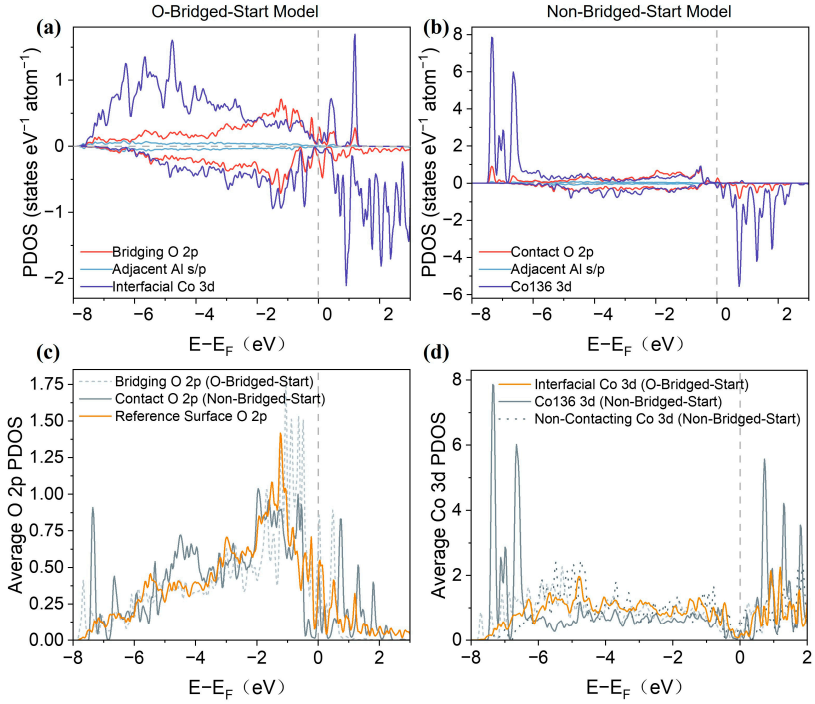


Figure 7. PDOS analysis of the relaxed CoO_x/Al_2O_3 interfaces: (**a**) O-bridged-start model, (**b**) non-bridged-start model, (**c**) spin-summed comparison of representative O sites, and (**d**) spin-summed comparison of representative Co sites. The vertical gray dashed line marks the Fermi level.

3.7. Occupied-State Bonding Through Shared Substrate Oxygen

As shown in Figure 8, ICOHP analyses were conducted to determine whether a substrate O atom can retain Al-O bonding while establishing new Co-O bonds in the O-bridged-start model. Figure 8a summarizes the bonding contributions of occupied states associated with the seven interfacial O atoms in the model. O69, O71, O77, O78, O81, O83, and O84 each show positive -ICOHP contributions on both the Al-O and Co-O sides. This pattern is in line with substrate-O-mediated coordination, in which a substrate O atom remains bonded to Al while forming an additional bond to Co.

The representative interfacial interactions were further evaluated against the complete Co-O and Al-O distributions obtained from the same LOBSTER calculation (Table 2). The 40 Co-O interactions internal to the CoO_x fragment are within a range of 2.07–8.30 eV. Twelve of these 40 intrafragment Co-O interactions have -ICOHP values greater than 5.48 eV. By contrast, the eight Co-O interactions are within a range of 2.01–5.48 eV. Thus, the Co-O interactions of the interface are not remarkably large relative to the Co-O interactions obtained using exactly the same electronic-structure projection. For Al-O, a similar internal comparison is possible. Across the substrate, the 249 Al-O interactions are within a range of 2.53–5.97 eV. Specifically, 72 Al-O bonds entirely in the bulk-like portion of the Al_2O_3 substrate are within a range of 3.12–4.83 eV. The representative interfacial Al28-O71 and Al28-O84 interactions have -ICOHP values of 4.55 and 4.82 eV, therefore lie within the range of the bulk-like portion of the substrate.

Table 2. Summary of -ICOHP values obtained in the study.

Interaction Group	Number	-ICOHP Range/Mean -ICOHP (eV)
Co-O within CoO_x fragment	40	2.07–8.30 (4.72)
Interfacial Co-O	8	2.01–5.48 (4.00)
Al-O within Al_2O_3 substrate	249	2.53–5.97 (3.98)
Al-O in the bulk-like portion	72	3.12–4.83 (4.19)

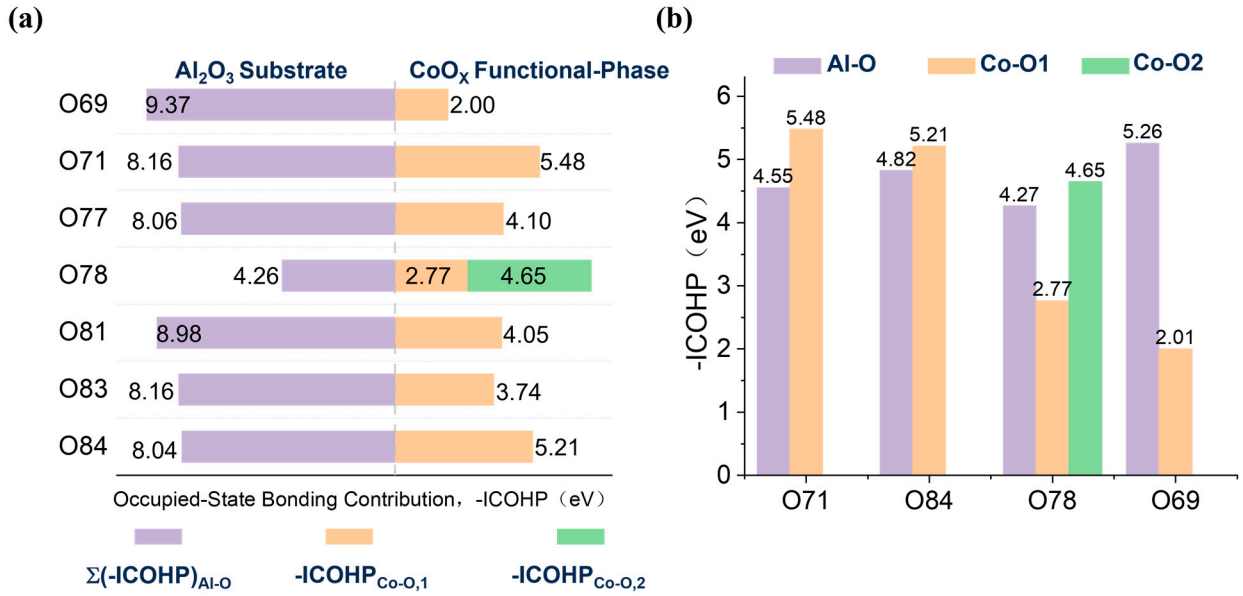


Figure 8. ICOHP analysis for the relaxed O-bridged-start model: (**a**) occupied-state bonding contributions on the Al-O and Co-O sides of each shared oxygen and (**b**) representative individual Al-O and Co-O interactions. Positive bars show the magnitude of -ICOHP.

Representative interactions are plotted in Figure 8b. O71 and O84, as representatives of strong bonding on both sides, have -ICOHP values of 5.48 and 4.55 eV for Co136-O71 and Al28-O71, respectively, while for Co142-O84 and Al28-O84, they are 5.21 and 4.82 eV, respectively. The important feature is not that these interactions are stronger than their bulk counterparts, but that the same O atom exhibits occupied-state bonding contributions toward both Al and Co. The sizable bonding contributions on both sides identify O71 and O84 as the O atoms in the Al_2O_3 substrate framework that also anchor interfacial Co. The bonding pattern at O78 indicates that there may be multi-center oxygen-mediated linkages. The -ICOHP values are 4.27, 2.77, and 4.65 eV for Al27-O78, Co136-O78, and Co139-O78, respectively, indicating occupied-state bonding to one Al atom and two Co atoms. The same connectivity can also be observed in the relaxed geometric structure. The O69 results show that the interfacial bonding strengths are unequal. Specifically, the -ICOHP value for Co145-O69 is only 2.01 eV. These ICOHP results show that the same surface O from the Al_2O_3 substrate can establish occupied-state Co-O bonding with interfacial Co while maintaining occupied-state Al-O bonding. The CoO_x layer and the Al_2O_3 support are therefore connected through substrate-O-mediated Co-O-Al bridges.

Taken together, site-specific FIB establishes a buried Co_3O_4/Al_2O_3 junction. STEM-EDS verifies the continuous distribution of oxygen, and HRTEM defines the local crystallographic relationship. The structures of the two initial models were relaxed. Charge-density differences and PDOS place the interfacial polarization and orbital coupling at substrate O sites, while ICOHP identifies occupied-state bonding from the same O atoms to both Al and Co.

4. Discussion

Unlike other modification methods, the sol–gel process is not the post-contact of formed Co_3O_4 particles, but the close adhesion between the undecomposed Co-containing precursor and virgin Al_2O_3 membranes. This enables the substrate O to participate in the coordination of metal sites, and the linkages will develop as the functional phases form. FIB specimen preparation provided access to such an O-mediated buried interface within the functionalized membrane. STEM-EDS and HRTEM analyses indicate contact between a

Co-rich spinel-type crystalline domain and Al_2O_3(012). The Co_3O_4 assignment is supported by the combined synthesis route and XRD bulk phase evidence. These observations favor a Co_3O_4-rich functional phase directly contacting Al_2O_3, although an ultrathin Al-containing interfacial reconstruction cannot be excluded. These results establish the physical junction and its local crystallographic relationship and provide experimental constraints for the subsequent DFT modeling.

After relaxation, the DFT calculations provide complementary atomistic evidence. Co-O-Al linkages form in both initial models, and the charge density response shows that configurations with more O-mediated connections exhibit a more widespread spatial distribution of interface charge rearrangement. The polarization of Co-O-Al connections from different models is of the same order of magnitude, and the total response intensity is primarily related to the number of connections. At the orbital level, the occupied Co 3d and substrate O 2p states exhibit substantial overlap, while no evident Co-Al hybridization is observed in the PDOS results. The ICOHP results also indicate that the same interfacial O atom remains bonded to Al while also forming a Co-O bond across the interface at the bond-resolved level. Importantly, comparison with all Co-O and Al-O interactions shows that the representative interfacial values are within the bonding distributions of the corresponding oxide components. The ICOHP results are evidence of shared-oxygen connectivity rather than stronger bonds. Together with the relaxed structures and PDOS results, these observations support substrate-O-mediated Co-O-Al linkages as the principal bonding motif at the interface.

Comparison of the two relaxed models suggests that the main difference is the extent of interfacial contact, not the presence or absence of oxygen bridges. After relaxation, the non-bridged-start model exhibits a localized Co-O-Al contact configuration, with three Co-O contacts concentrated around one interfacial Co site. In contrast, the O-bridged-start model exhibits a more extensively coordinated configuration, with eight Co-O contacts distributed across four interfacial Co sites. The results support the influence of the initial coordination number at the interface on the subsequent formation of Co-O-Al bonds, but do not imply the temporal progression from one structure to another.

Together, the FIB-HRTEM observations and DFT calculations integrate direct structural and multilevel evidence for interfacial chemical bonding without relying solely on element overlap, spectral peak analysis, or Co ion dissolution. It should be noted that this study focuses on the oxygen-bridging mode at heterogeneous oxide interfaces, rather than the dynamic description of interface formation processes. In addition, in future research, rigorous thermodynamic ranking of the interfacial configurations would require broader exploration of lateral registries, Co terminations and finite-temperature configurations.

From a functionalization perspective, synthesis conditions could be optimized by controlling alumina hydroxylation, precursor hydrolysis, and ligand-controlled surface reactions, and by selecting the thermal treatment conditions to promote the denser and more widely distributed network of interfacial Co-O-Al linkages [46–48]. In the future, further studies should elucidate how preparation conditions govern oxygen-bridging density.

5. Conclusions

In the field of coating and surface engineering, this research provides an atomic-level explanation for the chemical bonding between oxide phases derived from wet precursors and a porous ceramic membrane substrate. Based on the extraction of the real interface by FIB, STEM-EDS revealed a continuous O distribution across the Co-Al interface. HRTEM resolves a Co-rich spinel-type (111) lattice directly adjacent to Al_2O_3(012), while the predominant assignment to Co_3O_4 is further supported by the combined synthesis and XRD bulk phase. This local crystallographic relationship provides the experimental constraints

for DFT models. After structural relaxation, both initial models form Co-O-Al linkages. The O-bridged-start model forms eight interfacial contacts distributed across four Co sites, while the non-bridged-start model forms three contacts at a single Co site. More initial coordination numbers lead to a wider oxygen bridge structure and a greater overall charge redistribution. PDOS analysis shows orbital overlap between the Co 3d and O 2p states, whereas ICOHP results support both Al-O and Co-O bonding interactions involving the same substrate O atoms. Correlative FIB-HRTEM observations and DFT calculations reveal a laterally distributed network of Co-O-Al linkages at the interface and this shared-oxygen network provides a chemical anchoring mechanism between the Co_3O_4 functional layer and the porous Al_2O_3 substrate.

Author Contributions: Conceptualization, J.X. and W.Q.; methodology, J.X. and W.Q.; software, J.Y.; validation, J.X. and W.Q.; formal analysis, J.X. and W.Q.; investigation, J.X. and W.Q.; resources, J.Y.; data curation, J.X. and W.Q.; writing—original draft preparation, J.X. and W.Q.; writing—review and editing, J.X. and W.Q.; visualization, J.X. and W.Q.; supervision, J.X. and W.Q.; project administration, J.X. and W.Q.; funding acquisition, W.Q. All authors have read and agreed to the published version of the manuscript.

Funding: This research was funded by State Key Laboratory of Urban-rural Water Resources and Environment (Harbin Institute of Technology), grant number No. 2025DX23.

Institutional Review Board Statement: Not applicable.

Informed Consent Statement: Not applicable.

Data Availability Statement: The original contributions presented in this study are included in the article. Further inquiries can be directed to the corresponding author.

Acknowledgments: We are grateful for resources from the High-Performance Computing Center of Central South University.

Conflicts of Interest: The authors declare no conflicts of interest.

Appendix A

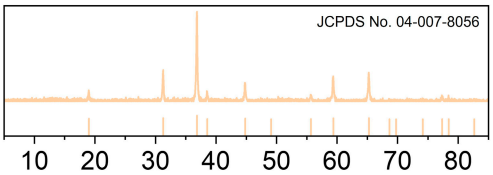


Figure A1. XRD of the bulk phase.

References

1. Morejudo, S.H.; Zanón, R.; Escolástico, S.; Yuste-Tirados, I.; Malerød-Fjeld, H.; Vestre, P.K.; Coors, W.G.; Martínez, A.; Norby, T.; Serra, J.M.; et al. Direct Conversion of Methane to Aromatics in a Catalytic Co-Ionic Membrane Reactor. *Science* **2016**, *353*, 563–566. [CrossRef] [PubMed]
2. Li, H.; Qiu, C.; Ren, S.; Dong, Q.; Zhang, S.; Zhou, F.; Liang, X.; Wang, J.; Li, S.; Yu, M. Na^+-Gated Water-Conducting Nanochannels for Boosting CO_2 Conversion to Liquid Fuels. *Science* **2020**, *367*, 667–671. [CrossRef] [PubMed]
3. Zhao, Y.; Sun, M.; Wang, X.; Wang, C.; Lu, D.; Ma, W.; Kube, S.A.; Ma, J.; Elimelech, M. Janus Electrocatalytic Flow-through Membrane Enables Highly Selective Singlet Oxygen Production. *Nat. Commun.* **2020**, *11*, 6228. [CrossRef] [PubMed]
4. Gu, Q.; Ng, T.C.A.; Bao, Y.; Ng, H.Y.; Tan, S.C.; Wang, J. Developing Better Ceramic Membranes for Water and Wastewater Treatment: Where Microstructure Integrates with Chemistry and Functionalities. *Chem. Eng. J.* **2022**, *428*, 130456. [CrossRef]
5. Duan, Y.; Wang, R.; Shocron, A.N.; Elimelech, M. Design Principles of Catalytic Reactive Membranes for Water Treatment. *Nat. Water* **2025**, *3*, 949–962. [CrossRef]

6. Yang, Y.; Li, H.; Fu, W.; Hu, Z.; Yang, R.; Xu, H.; Chang, Q.; Wang, Q.; Wang, Y.; Chen, X.; et al. Large-Scale Deployment of Single-Atom Catalysts via Cross-Scale Confinement in Ceramic Membranes for Advanced Water Treatment. *Nat. Water* **2025**, *3*, 1281–1290. [CrossRef]
7. He, Z.; Ong, J.H.; Bao, Y.; Hu, X. Chemocatalytic Ceramic Membranes for Removing Organic Pollutants in Wastewater: A Review. *J. Environ. Chem. Eng.* **2023**, *11*, 109548. [CrossRef]
8. Gong, Y.; Wu, Y.; Shen, J.; Zhao, S.; Xu, X.; Kang, J.; Shen, L.; Zhou, Y.; Zhao, Y.; Chen, Z. Generation of Interfacial High-Spin Manganese Intermediates as Reactive Oxidant During Peroxymonosulfate Activation Mediated by Amorphous MnO_x Supported on Polymeric Substrate. *Appl. Catal. B Environ.* **2022**, *316*, 121671. [CrossRef]
9. Hou, X.; Wang, H.; Jia, L.; Li, M.; Yu, W.; Bian, Z. Nitrogen-Doped Carbon Bilayer Flow-Through Electrocatalytic Membrane Based on Transition Metal Single Atoms: Simultaneous Generation and Activation of H_2O_2 for Ibuprofen Degradation. *Chem. Eng. J.* **2025**, *513*, 162950. [CrossRef]
10. Hesaraki, S.A.H.; Önal, B.; Prymak, O.; Ren, Z.; Ulbricht, M.; Fischer, L. Material-Efficient Synthesis of Polymer Membrane-Immobilized Metal Oxides for Advanced Oxidation Processes: Catalytic Mechanism, Stability and Performance. *Small* **2025**, *21*, e07532. [CrossRef] [PubMed]
11. Bai, Z.; Gao, S.; Yu, H.; Liu, X.; Tian, J. Layered Metal Oxides Loaded Ceramic Membrane Activating Peroxymonosulfate for Mitigation of NOM Membrane Fouling. *Water Res.* **2022**, *222*, 118928. [CrossRef] [PubMed]
12. Fan, Y.; Zhou, Y.; Feng, Y.; Wang, P.; Li, X.; Shih, K. Fabrication of Reactive Flat-Sheet Ceramic Membranes for Oxidative Degradation of Ofloxacin by Peroxymonosulfate. *J. Membr. Sci.* **2020**, *611*, 118302. [CrossRef]
13. Tsiarta, N.; Morović, S.; Mandić, V.; Panžić, I.; Blažic, R.; Ćurković, L.; Gernjak, W. Catalytic Ozonation of Pharmaceuticals Using CeO_2-$CeTiO_x$-Doped Crossflow Ultrafiltration Ceramic Membranes. *Nanomaterials* **2024**, *14*, 1163. [CrossRef] [PubMed]
14. Li, A.; Liu, Y.; Wang, Z.; Song, Z.; Zhang, Y.; Wang, Y.; Xu, B.; Qi, F.; Ikhlaq, A.; Kumirska, J.; et al. Catalytic Ozonation Membrane Reactor Integrated with $CuMn_2O_4$/rGO for Degradation Emerging UV Absorbers (BP-4) and Fouling In-Situ Self-Cleaning. *Sep. Purif. Technol.* **2021**, *279*, 119804. [CrossRef]
15. Zhao, P.; Gao, Y.; Xu, G.; Zhang, E.; Liu, L.; Jin, S. Fabrication of $Cu_{1.4}Mn_{1.6}O_4$ Modified Catalytic Ozonation Ceramic Membrane for Membrane Fouling Elimination and Micro-Pollutant Degradation. *J. Am. Ceram. Soc.* **2023**, *106*, 4089–4102. [CrossRef]
16. Xu, P.; Wei, R.; Wang, P.; Shen, T.; Zheng, T.; Zhang, G. A Nanoconfined $FeCo_2O_4$-Embedded Ceramic Membrane Regulates Electron Transfer in Peroxymonosulfate Activation to Selectively Generate Singlet Oxygen for Water Decontamination. *Environ. Sci. Technol.* **2024**, *58*, 17464–17474. [CrossRef] [PubMed]
17. Zhang, Y.; Yip, K.L.; Kim, Y.; Chouinard, C.; Licato, J.; Kim, J.-H. Monolithic Ceramic $CoTiO_3$/TiO_2 Membrane Balancing Catalytic Efficiency and Durability in Advanced Oxidation Processes. *Environ. Sci. Technol.* **2025**, *59*, 6863–6871. [CrossRef] [PubMed]
18. Zhou, M.; Yang, Q.; Troczynski, T. Effect of Substrate Surface Modification on Alumina Composite Sol–Gel Coatings. *Surf. Coat. Technol.* **2006**, *200*, 2800–2804. [CrossRef]
19. Wang, Y.; Zhao, S.; Fan, W.; Tian, Y.; Zhao, X. The Synthesis of Novel Co–Al_2O_3 Nanofibrous Membranes with Efficient Activation of Peroxymonosulfate for Bisphenol a Degradation. *Environ. Sci. Nano* **2018**, *5*, 1933–1942. [CrossRef]
20. Wan, Z.; Chae, S.H.; Meese, A.F.; Nwokonkwo, O.; Arrazolo, L.; Yip, K.L.; Ma, X.; Liu, S.; Muhich, C.; Wang, D.; et al. Overcoming the Reactivity-Stability Challenge in Water Treatment Catalyst Through Spatial Confinement. *Nat. Commun.* **2025**, *16*, 9672. [CrossRef]
21. Huber, F.; Berwanger, J.; Polesya, S.; Mankovsky, S.; Ebert, H.; Giessibl, F.J. Chemical Bond Formation Showing a Transition from Physisorption to Chemisorption. *Science* **2019**, *366*, 235–238. [CrossRef]
22. Bao, Y.; Lee, W.J.; Lim, T.-T.; Wang, R.; Hu, X. Pore-Functionalized Ceramic Membrane with Isotropically Impregnated Cobalt Oxide for Sulfamethoxazole Degradation and Membrane Fouling Elimination: Synergistic Effect Between Catalytic Oxidation and Membrane Separation. *Appl. Catal. B Environ.* **2019**, *254*, 37–46. [CrossRef]
23. Liu, S.; Li, K.; Hughes, R. Preparation of Porous Aluminium Oxide (Al_2O_3) Hollow Fibre Membranes by a Combined Phase-Inversion and Sintering Method. *Ceram. Int.* **2003**, *29*, 875–881. [CrossRef]
24. Nyathi, T.M.; Fischer, N.; York, A.P.E.; Morgan, D.J.; Hutchings, G.J.; Gibson, E.K.; Wells, P.P.; Catlow, C.R.A.; Claeys, M. Impact of Nanoparticle–Support Interactions in Co_3O_4/Al_2O_3 Catalysts for the Preferential Oxidation of Carbon Monoxide. *ACS Catal.* **2019**, *9*, 7166–7178. [CrossRef]
25. Jongsomjit, B.; Panpranot, J.; Goodwin, J.G. Co-Support Compound Formation in Alumina-Supported Cobalt Catalysts. *J. Catal.* **2001**, *204*, 98–109. [CrossRef]
26. Greczynski, G.; Pshyk, O.; Hultman, L. Toward an Increased Reliability of Chemical Bonding Assignment in Insulating Samples by X-Ray Photoelectron Spectroscopy. *Sci. Adv.* **2023**, *9*, eadi3192. [CrossRef]
27. Biesinger, M.C.; Payne, B.P.; Grosvenor, A.P.; Lau, L.W.M.; Gerson, A.R.; Smart, R.S.C. Resolving Surface Chemical States in XPS Analysis of First Row Transition Metals, Oxides and Hydroxides: Cr, Mn, Fe, Co and Ni. *Appl. Surf. Sci.* **2011**, *257*, 2717–2730. [CrossRef]

28. Zhukovskii, Y.F.; Kotomin, E.A.; Herschend, B.; Hermansson, K.; Jacobs, P.W.M. A First-Principles Study of the Ag/a-Al_2O_3(0001) Interface. *Int. J. Mol. Sci.* **2001**, *2*, 271–280. [CrossRef]
29. Kresse, G.; Furthmüller, J. Efficient Iterative Schemes for Ab Initio Total-Energy Calculations Using a Plane-Wave Basis Set. *Phys. Rev. B* **1996**, *54*, 11169–11186. [CrossRef] [PubMed]
30. Kresse, G.; Furthmüller, J. Efficiency of Ab-Initio Total Energy Calculations for Metals and Semiconductors Using a Plane-Wave Basis Set. *Comput. Mater. Sci.* **1996**, *6*, 15–50. [CrossRef]
31. Catalano, J.G.; Park, C.; Zhang, Z.; Fenter, P. Termination and Water Adsorption at the α-Al_2O_3 (012)−Aqueous Solution Interface. *Langmuir* **2006**, *22*, 4668–4673. [CrossRef]
32. Hütner-Reisch, J.I.; Conti, A.; Kugler, D.; Mittendorfer, F.; Schmid, M.; Diebold, U.; Balajka, J. AFM Imaging Reveals the Unreconstructed α-Al_2O_3(0001) Surface to Be Inhomogeneous and Rough. *Nat. Commun.* **2026**, *17*, 4692. [CrossRef]
33. Blöchl, P.E. Projector Augmented-Wave Method. *Phys. Rev. B* **1994**, *50*, 17953–17979. [CrossRef]
34. Kresse, G.; Joubert, D. From Ultrasoft Pseudopotentials to the Projector Augmented-Wave Method. *Phys. Rev. B* **1999**, *59*, 1758–1775. [CrossRef]
35. Perdew, J.P.; Burke, K.; Ernzerhof, M. Generalized Gradient Approximation Made Simple. *Phys. Rev. Lett.* **1996**, *77*, 3865–3868. [CrossRef] [PubMed]
36. Dudarev, S.L.; Botton, G.A.; Savrasov, S.Y.; Humphreys, C.J.; Sutton, A.P. Electron-Energy-Loss Spectra and the Structural Stability of Nickel Oxide: An LSDA+U Study. *Phys. Rev. B* **1998**, *57*, 1505–1509. [CrossRef]
37. Wang, L.; Maxisch, T.; Ceder, G. Oxidation Energies of Transition Metal Oxides within the GGA+U Framework. *Phys. Rev. B* **2006**, *73*, 195107. [CrossRef]
38. Li, Q.; Wu, J.; Yao, Z.; Xu, Y.; Thackeray, M.M.; Wolverton, C.; Dravid, V.P. Dynamic Imaging of Metastable Reaction Pathways in Lithiated Cobalt Oxide Electrodes. *Nano Energy* **2018**, *44*, 15–22. [CrossRef]
39. Bellomi, S.; Cano-Blanco, D.C.; Han, Y.; Delgado, J.J.; Chen, X.; Lomachenko, K.A.; Barlocco, I.; Ferri, D.; Roldan, A.; Villa, A. Understanding the Interfacial Changes of $PtCo_3O_4$ Catalysts During the Dehydrogenation of Ammonia Borane. *Appl. Surf. Sci.* **2025**, *711*, 164116. [CrossRef]
40. Dronskowski, R.; Bloechl, P.E. Crystal Orbital Hamilton Populations (COHP): Energy-Resolved Visualization of Chemical Bonding in Solids Based on Density-Functional Calculations. *J. Phys. Chem.* **2002**, *97*, 8617–8624.
41. Maintz, S.; Deringer, V.L.; Tchougréeff, A.L.; Dronskowski, R. LOBSTER: A Tool to Extract Chemical Bonding from Plane-Wave Based DFT. *J. Comput. Chem.* **2016**, *37*, 1030–1035. [CrossRef]
42. Bolt, P.H.; Habraken, F.H.P.M.; Geus, J.W. Formation of Nickel, Cobalt, Copper, and Iron Aluminates from α- and γ-Alumina-Supported Oxides: A Comparative Study. *J. Solid State Chem.* **1998**, *135*, 59–69. [CrossRef]
43. Grzybek, G.; Ciura, K.; Wójcik, S.; Gryboś, J.; Indyka, P.; Inger, M.; Antoniak-Jurak, K.; Kowalik, P.; Kotarba, A.; Sojka, Z. On the Selection of the Best Polymorph of Al_2O_3 Carriers for Supported Cobalt Nano-Spinel Catalysts for N_2O Abatement: An Interplay between Preferable Surface Spreading and Damaging Active Phase–Support Interaction. *Catal. Sci. Technol.* **2017**, *7*, 5723–5732. [CrossRef]
44. Vaz, C.A.F.; Henrich, V.E.; Ahn, C.H.; Altman, E.I. Growth and Characterization of Thin Epitaxial Co_3O_4(111) Films. *J. Cryst. Growth* **2009**, *311*, 2648–2654.
45. Chizallet, C.; Schlaup, C.; Fonda, E.; Carrier, X. Surface Orientation Dependent Interaction of Cobalt (II) Precursors with Alpha-Alumina. *J. Catal.* **2021**, *394*, 157–166. [CrossRef]
46. Cherepanova, S.V.; Koemets, E.G.; Gerasimov, E.Y.; Simentsova, I.I.; Bulavchenko, O.A. Reducibility of Al^{3+}-Modified Co_3O_4: Influence of Aluminum Distribution. *Materials* **2023**, *16*, 6216. [CrossRef]
47. Byun, S.W.; Shin, H.; Bin Bae, W.; Hazlett, M.J.; Jin Kim, Y.; Jun Lee, S.; Kim, M.; Bong Kang, S. Dry Synthesis of Alumina-Supported Cobalt Catalyst for Highly Enhanced Catalytic Oxidation. *Chem. Eng. J.* **2024**, *481*, 148316. [CrossRef]
48. Backman, L.B.; Rautiainen, A.; Lindblad, M.; Krause, A.O.I. The Interaction of Cobalt Species with Alumina on Co/Al_2O_3 Catalysts Prepared by Atomic Layer Deposition. *Appl. Catal. A Gen.* **2009**, *360*, 183–191. [CrossRef]

Disclaimer/Publisher's Note: The statements, opinions and data contained in all publications are solely those of the individual author(s) and contributor(s) and not of MDPI and/or the editor(s). MDPI and/or the editor(s) disclaim responsibility for any injury to people or property resulting from any ideas, methods, instructions or products referred to in the content.